Corrosion Science 258 (2026) 113450

Contents lists available at ScienceDirect

Corrosion Science

journal homepage: www.elsevier.com/locate/corsci

Data-driven high-throughput screening of Fe-Cr-Mo-C-B amorphous alloy with excellent corrosion and wear resistance

Fangkai Xiong [a], Gaopeng Zou [a], Yuxi Qi [a], Bo Sun [a], Baosen Zhang [b], Shuaishuai Zhu [b], Tao Liang [c], Qiaoshi Zeng [c], Xuhai Zhang [a], Qianqian Wang [a,*], Baolong Shen [a,*]

[a] School of Materials Science and Engineering, Jiangsu Key Laboratory for Advanced Metallic Materials, Southeast University, Nanjing 211189, China
[b] School of Materials Science and Engineering, Jiangsu Key Laboratory of Advanced Structural Materials and Application Technology, Nanjing Institute of Technology, Nanjing 211167, China
[c] Center for High Pressure Science and Technology Advanced Research, Shanghai 201203, China

ARTICLE INFO

Dataset link: Original data

Keywords:
Fe-Cr-Mo-C-B
Amorphous alloy
High-throughput
Corrosion resistance
Machine learning

ABSTRACT

Fe-based amorphous coatings are widely used as surface protection materials due to their excellent corrosion resistance. However, the complex elemental combinations and vast composition space of Fe-based amorphous alloys present significant challenges in material optimization. In this study, combinatorial fabrication, high-throughput characterization, and machine learning were employed to systematically investigate the Fe-Cr-Mo-C-B amorphous alloy system, which incorporates key elements commonly used in Fe-based amorphous coatings. A material library comprising 69 compositions was synthesized via magnetron co-sputtering, and the effects of alloy composition on glass-forming ability (GFA), corrosion resistance, and hardness were systematically analyzed. Machine learning using a random forest regression (RFR) model was applied to expand the dataset to 690 compositions. The results indicated that corrosion resistance strongly depends on the concentrations of Fe and Cr, with Mo playing a critical role in enhancing GFA. Furthermore, excessive Cr content led to the formation of Cr-poor and Cr-rich regions, increasing susceptibility to corrosion. $Fe_{31}Cr_{31}Mo_{14}C_{14}B_{10}$, with outstanding comprehensive properties, including good corrosion resistance, high hardness, large GFA, and excellent stability, was used for coating preparation using the high-velocity oxygen fuel (HVOF) method. The coating exhibited excellent overall performance, including corrosion potential of -0.34 $V_{Ag/AgCl}$, corrosion current density of $1.4 \times 10^{-7} A/cm^2$, and ultra-low wear rate of 6×10^{-7} $mm^3N^{-1}m^{-1}$. These findings highlight the potential of integrating high-throughput experiments with machine learning to accelerate the discovery and design of Fe-based amorphous alloys with optimized corrosion and wear resistance.

1. Introduction

Corrosion and wear of metallic materials severely impair marine equipment's reliability and service life. Amorphous alloys are well-known for their outstanding corrosion and wear resistance compared to traditional crystalline alloys due to their long-range disordered atomic arrangement without crystalline defects [1–7]. Among the various systems of amorphous alloys, Fe-based amorphous alloys have drawn significant attention due to their high strength, excellent corrosion resistance, and low production costs [8,9]. Preparing Fe-based amorphous coatings using additive manufacturing technology, including thermal spraying, laser cladding, and cold spraying, is considered as a promising surface protective route for marine equipment [2,10]. In 2003, the US navy started HPCRM program and NACCA program, and announced $Fe_{48}Cr_{15}Mo_{14}C_{15}B_6Y_2$ (SAM1651) and $Fe_{49.7}Cr_{17.7}Mn_{1.9}Mo_{7.4}W_{1.6}B_{15.2}C_{3.8}Si_{2.4}$ (SAM2X5) amorphous coatings with excellent corrosion, wear and radiation resistance, and demonstrated application cases as stable and reliable protection for nuclear waste storage [11–13]. Since then, many research groups have been working on composition modification, heat treatment, and spray process analyses of the coatings. However, the composition of most reported Fe-based amorphous coatings stayed with SAM1651 and SAM2X5, or just minor variations from the original composition. Therefore, developing Fe-based amorphous coatings with novel compositions that have higher corrosion and wear resistance is important for the surface protection of marine equipment.

* Corresponding authors.
E-mail addresses: qwang678@seu.edu.cn (Q. Wang), blshen@seu.edu.cn (B. Shen).

https://doi.org/10.1016/j.corsci.2025.113450
Received 11 March 2025; Received in revised form 25 May 2025; Accepted 27 October 2025
Available online 28 October 2025

The effects of both the metallic elements and metalloids on the structure and properties of Fe-based amorphous coatings have been extensively investigated. For example, Xu et al. reported that as the Cr content in $Fe_{79.5-x}Si_{9.5}B_{11}Cr_x$ alloys increases from 0 to 5 at%, the corrosion rate of the alloys in 0.1 M NaCl solution decreases from 1.83×10^{-1} to 3.91×10^{-4} mm·year^{-1} [14]. Maddala et al. found that alloying an Fe-Cr-Mo-C-B system with 2 at% Er resulted in a ~55 % improvement in the wear resistance [15]. Li et al. focused on SAM1651 and developed a series of novel Fe-based bulk amorphous alloys with improved wear resistance by altering the Cr and Mo contents in $Fe_{77-x-y}Cr_xMo_yC_{15}B_6Y_2$ system [16]. However, the vast composition space of possible elemental combinations in multicomponent alloys makes it extremely time-consuming and challenging to explore and discover high-performance amorphous alloys by traditional methods [17]. In order to develop novel Fe-based amorphous coatings with better corrosion and wear properties, a comprehensive screening of the metallic elements and metalloids on the corrosion and wear properties of the Fe-based amorphous coatings is needed. Fe, Cr, Mo, C, and B, as the primary constituents of the SAM1651 alloy, and also the most commonly used elements in the Fe-based amorphous coatings, play a critical role in achieving outstanding comprehensive properties in terms of corrosion resistance, glass-forming ability and wear resistance. Understanding how these elements affect microstructure and properties is essential for optimizing the performance of Fe-based amorphous coatings.

The high-throughput design of materials, including combinatorial synthesis and high-throughput characterization, has been proposed for developing novel compositionally complex alloys with outstanding properties [18–21]. For instance, Li et al. fabricated a large compositional library through magnetron co-sputtering and established the relationship between GFA and electrical resistivity for Ir-Ni-Ta alloy material library via sheet resistance measurements [9]. Further analysis of the X-ray diffraction (XRD) patterns of over 5700 alloys revealed that the width of the first XRD peak (FWHM) varies regularly with composition,the wider FWHM corresponds to the larger GFA [22]. Recently, the corrosion resistance of the prepared Ir-Ni-Ta material library has been characterized, revealing that alloy composition is the decisive factor in corrosion resistance [23]. Shi et al. synthesized an $Al_x(CoCrFeNi)_{100-x}$ high-entropy alloy material library using magnetron co-sputtering, dividing it into ten equal parts along the composition gradient and conducting electrochemical measurements in a 3.5 wt% NaCl solution to investigate the effect of Al content on corrosion resistance [24]. However, although Fe-based amorphous alloys are the most widely used system among the amorphous alloys, little high-throughput synthesis or characterization has been reported on the Fe-based amorphous materials.

Recently, data-driven machine learning techniques have demonstrated remarkable success in modeling and predicting material properties, owing to their ability to manage complex data and high efficiency, outperforming traditional analytical methods [25,26]. For instance, Guo et al. utilized a neural network model to determine the optimal FeCoBSiCu alloy within a composition space of 486,000 permutations and combinations, significantly accelerating the material development process [27]. Similarly, Liu et al. employed clustering and Random Forest (RF) models to rapidly design high-performance non-oriented silicon steel, achieving target performance based on a small dataset [28]. Lee et al. integrated high-throughput preparation and characterization with machine learning to quickly establish the relationship between GFA and electrical resistivity, thus identifying characteristic parameters that describe the electrical resistivity of alloy amorphous formation [29]. High-throughput experiments generate large volumes of data, providing a reliable and substantial dataset for machine learning. By combining high-throughput experiments with machine learning, the efficiency of developing new Fe-based amorphous alloys can be further enhanced.

In this study, a Fe-Cr-Mo-C-B material library comprising 69 compositions was prepared using a high-throughput magnetron co-sputtering approach. The composition, microstructure, GFA, corrosion resistance, and hardness of the samples were systematically analyzed, revealing the internal relationships between elemental influence and the properties. Machine learning was employed to predict alloy compositions with excellent corrosion resistance and high GFA, enabling accurate predictions and efficient optimization of performance metrics. To validate the predictions, ribbon, rod, and coating samples were fabricated and analyzed. This work provides a valuable reference for the development of Fe-based amorphous coatings with excellent corrosion and wear resistance utilizing high-throughput methodologies and data-driven machine learning for industrial surface protection applications.

2. Experiment

2.1. Sample preparation

The Fe-Cr-Mo-C-B alloy material library was fabricated via magnetron co-sputtering using an FJL-560a magnetron sputtering system. The desired compositional range of the library was achieved by altering the orientation angles of the sputtering targets relative to the substrate, and tuning the sputtering power applied to the targets [30], as shown in Fig. 1 (Fig. 1a is a schematic diagram of magnetron co-sputtering, while Fig. 1b shows a schematic of the original sample platform before attaching the silicon wafer.). $Fe_{80}C_{10}B_{10}$, $Cr_{80}C_{10}B_{10}$ and $Mo_{80}C_{10}B_{10}$ (at %) alloys, manufactured by hot press sintering with a purity higher than 99.9 %, were used as sputtering targets, and the dimensions of the targets were 60 × 3 mm. Polished 4-inch Si wafers were cut into 8 mm × 8 mm × 0.5 mm substrates using a diamond scribe and used for film deposition. After deposition, the samples were further diced in half to expose the cross-section for SEM characterization. The base pressure of the chamber was lower than 1×10^{-4} Pa, and a working pressure of 0.5 Pa was maintained by flowing high-purity argon during sputtering. No intentional heating or cooling was applied to the substrates during deposition. The applied sputtering power of $Fe_{80}C_{10}B_{10}$, $Cr_{80}C_{10}B_{10}$ and $Mo_{80}C_{10}B_{10}$ targets were 130 W (DC), 110 W (DC pulse), and 50 W (DC pulse), respectively. To prepare ribbon and rod samples, alloy ingots were fabricated by induction melting in an argon atmosphere. Ribbon samples were produced using the single-roller melt spinning technique with a wheel speed of approximately 40 m/s, while rod samples were prepared via copper mold casting. $Fe_{31}Cr_{31}Mo_{14}C_{14}B_{10}$ (at%) amorphous powders were synthesized through gas atomization with high-purity argon using industrial-grade raw materials. Powders with a particle size of less than 53 μm were used as feedstock for the thermal spraying of Fe-based amorphous coatings onto 304 stainless steel substrates. The coatings were prepared using a HVOF thermal spray system (HD-8000). The preparation parameters of the HVOF coating are provided in Table S1. To distinguish between different sample types, suffixes were assigned: for instance, Cr31-film for film samples with Cr content of 31 at%, Cr31-ribbon for ribbon samples, Cr31-rod for rod samples, Cr31-powder for powder samples, and Cr-31-coating for coating samples.

2.2. Structure characterization

The compositions of Fe-Cr-Mo-C-B films were analyzed using an electron probe X-ray micro-analyzer (EPMA, 1720 H), with atomic number-absorption-fluorescence (ZAF) correction. High-purity Fe, Cr, Mo, C, and B elemental standards (purity > 99.99 %) were used, and a thin-film fitting model was applied. Measurements were performed at the central region of each sample to ensure consistency. And the surface and cross-section morphologies were analyzed by scanning electron microscopy (SEM, Navo Nano SEM450). The thickness of all the sputtered films was measured using profilometer (DEKTAK 150). The phase mapping of the films was analyzed using X-ray diffraction (XRD, SmartLab μ) with Cu Kα radiation, with a scanning range from 30° to

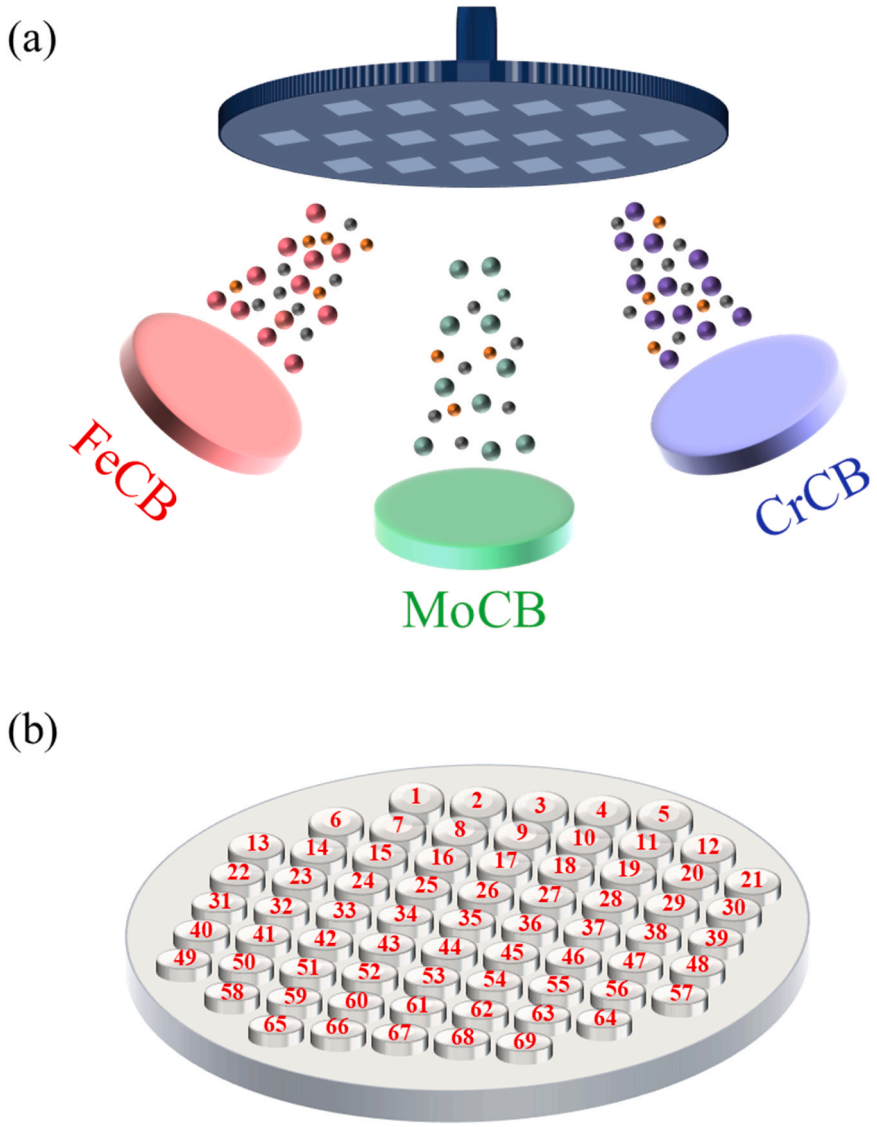

Fig. 1. A schematic diagram of the magnetron co-sputtering system used to prepare the Fe-Cr-Mo-C-B material libraries. (a) Schematic diagram of magnetron co-sputtering. (b) Schematic of the original sample platform before attaching the silicon wafer.

80°. The spot size was 70 μm, and 69 points were selected within a 4-inch diameter region. The phases of the ribbon, rod, powder, and coating samples were analyzed by X-ray diffraction (XRD, Ultima IV) using Cu Kα radiation, with a scanning range from 30° to 80°. The nanostructure of the films was analyzed via transmission electron microscopy (TEM, Talos F200X) coupled with energy-dispersive X-ray spectroscopy (EDS). The TEM samples were prepared by a focused ion beam (FIB, Helios 5 CX DualBeam). The chemical composition and oxidation state of passive films on the surface of films were analyzed using X-ray photoelectron spectroscopy (XPS, Thermo Scientific K-Alpha) with Al Kα excitation. The XPS spectra were calibrated according to the difference between the experimental carbon 1 s peak and the standard carbon 1 s (284.8 eV). The standard binding energies of Fe 2p, Cr 2p, Mo 3d, and C 1 s were referred to the NIST XPS database. The XPS spectra were acquired with a pass energy of 50 eV, an accelerating voltage of 12 kV, and a spot size of 400 μm. Thermal properties, including glass transition temperature (T_g), crystallization temperature (T_x), and supercooled liquid region ($\triangle T_x = T_x\text{-}T_g$), were measured using differential scanning calorimetry (DSC, NETZSCH DSC404F3) at a heating rate of 0.67 K/s.

2.3. Electrochemical measurements

Electrochemical tests of the film and ribbon samples were conducted in 3.5 wt% NaCl solution at room temperature using a CHI660 electrochemical workstation. A standard three-electrode configuration was employed, consisting of a platinum counter electrode, an Ag/AgCl reference electrode, and the sample as the working electrode. For comparison, a 304 stainless steel sample (the detailed composition is listed in Table S2.) was also tested under the same conditions. The exposed area of the working electrode was approximately 0.24 cm^2. Electrochemical impedance spectroscopy (EIS) measurements were performed after a 20 min exposure to the solution at room temperature. A sinusoidal perturbation of 10 mV (rms) was applied over a frequency range of 100 kHz to 0.01 Hz. And then potentiodynamic polarization curves were recorded at a scan rate of 5 mV/s. The corrosion potential (E_{corr}) and corrosion current density (i_{corr}) were determined via Tafel extrapolation. The passive current density (i_{pass}) was defined as the stabilized current density measured at 0.2 V (vs. Ag/AgCl) within the passive region, as illustrated in Fig. S1. All measurements were performed in individual electrolyte cells to avoid cross-contamination, and the same sample was used for both EIS and polarization measurements.

The potentiostatic polarisation tests were conducted at 1 $V_{Ag/AgCl}$ to examine the stability of passive films.

2.4. Mechanical tests

Nanoindentation tests were carried out on the film samples using a Nanoindentation system (Agilent G200). The reduced modulus (E_r) and hardness (H) were measured with partial unloading mode for each cycle increases gradually to 1000 nm. To eliminate the substrate influence, the indentation depth was set as 70–120 nm. 6 indentations were carried out on each sample to obtain average hardness. For wear tests, the coatings were ground using 2000-grit silicon carbide paper and then polished with 0.25 μm diamond pastes. The counterpart was a Si_3N_4 ball of 12.7 mm in diameter. The reciprocating distance was 2 mm. The applied normal contact load of the corrosion-wear tests was 20 N, the sliding speed was 30 mm/s with a stroke frequency of 5 Hz, and the test period was 20 min. The bending profile of the film and substrate was measured by profilometer (DEKTAK 150).

2.5. Machine learning

Random Forest Regression (RFR) model was employed to predict the E_{corr}, i_{corr} and the full width at half maximum (FWHM) of the XRD diffraction peaks of the alloys. The typical structure of an RFR model consists of data preparation, model training, and ensemble prediction, as shown in Fig. S2. The compositions of all five elements (Fe, Cr, Mo, C, and B) and corresponding performance data obtained from high-throughput experiments were used as the training dataset. The bootstrap technique was employed to sample the dataset and construct multiple decision trees, with results aggregated through majority voting or averaging, thereby enhancing prediction accuracy and robustness. The model inputs were the atomic percentages of each element, while the outputs were the corresponding performance metrics. To prevent overfitting, the dataset was split randomly into 80 % for training and 20 % for testing. Mean squared error (MSE) was used to evaluate prediction performance, and similar values for training and testing indicate minimal overfitting. Additionally, the trained model was applied to predict E_{corr}, i_{corr}, and FWHM for the original 69 data points, which showed strong consistency with the experimental results. Two hyperparameters, the minimum samples required to split a node and the minimum samples required at a leaf node, were set to 2 and 1, respectively, ensuring sufficiently small tree branches and leaf nodes. The training process utilized cross-validation to ensure that both the training and testing sets adequately represented the entire dataset.

3. Results and discussion

3.1. High-throughput screening of the combinational materials library

Fig. 2a displays a photograph of a representative Fe-Cr-Mo-C-B materials library comprising 69 alloys in the form of thin films. The composition at the center of each film was determined using EPMA. Fig. 2b-f present the contour plots of the elemental concentrations, with the corresponding data of 69 samples summarized in Table S3. The compositional spread of the library can be tuned by the source-to-substrate orientation and target power settings. The compositional range of the combinatorial materials library spans 17–55 at% for Fe, 12–49 at% for Cr, 9–18 at% for Mo, 12–16 at% for C, and 8–11at% for B. The compositional variation within a single sample is shown in Table S3, and the deviation is less than 5 %. According to literature, the contents of Fe, Cr, Mo, C, and B in the reported Fe-based amorphous alloy coatings are within the above composition range [2]. According to the contour plots, the metallic element content decreases as the distance from the target increases. As the concentration of C and B elements on each target is the same, the metalloids element contents of the samples only exhibit minor change.

The surface and cross-sectional morphologies of the as-deposited films were analyzed by SEM, with representative results shown in Fig. S3. The surface of all films exhibited smooth and dense morphologies under SEM, with no visible grains or defects, suggesting an amorphous-like structure, consistent with previously reported amorphous films prepared via magnetron sputtering. The cross section of the films are typical morphologies showing the growth direction of the film [31]. No apparent defects, such as pores or cracks, were observed. The film thickness ranged from approximately 1.6–1.9 μm, and the variations within the magnetron co-sputtering library were attributed to the

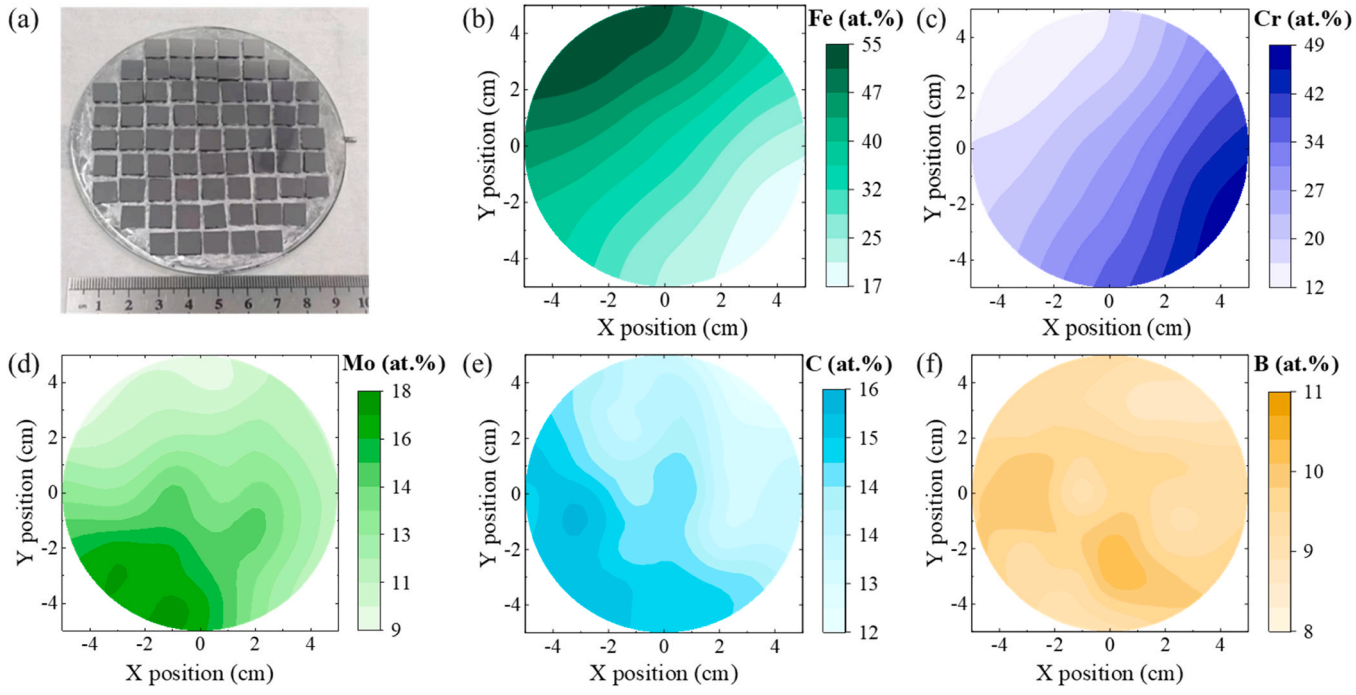

Fig. 2. (a) Photograph of materials library. (b-f) Contour plots for the concentration of Fe, Cr, Mo, C, B, respectively.

source-to-substrate orientation and target power settings. To investigate the potential influence of residual stresses introduced during sputtering on subsequent performance tests, the residual stresses of Cr12-film and Cr44-film (#6 and #64 samples as shown in Fig. 1b), which have the largest difference in Fe/Cr content, and also the largest distance on the sample stage, were measured, as illustrated in Fig. S4. The results revealed only a minor difference in residual stresses between the two films, suggesting that the impact of residual stresses on subsequent performance evaluations can be considered negligible.

The phase structure of the 69 film samples was analyzed using XRD mapping, with the results shown in Fig. 3a, and a representative XRD curve of sample #8 (randomly picked) is displayed in Fig. 3b. The XRD pattern of the sample #8 consists a broad diffusive peak and a sharp diffraction peak representing Si (100) at 69°, indicating that the film is amorphous. As the strong diffraction peak from Si (001) makes the diffusive peak from the film seem inconspicuous, the XRD mapping results in Fig. 3a only presented results at 30–60° for 2θ. All of the 69 samples exhibit only a diffusive diffraction peak, revealing their amorphous structure. This is probably due to the high cooling rate of sputtering [32]. The FWHM of the broad diffraction peaks was calculated to characterize the GFA of the films. It has been suggested that there is a strong correlation between GFA and FWHM, as alloys with larger FWHM values tend to have higher structural disorder, which is beneficial for glass formation [22]. Fig. 3c utilizes the contour plot to show the variation of FWHM for the as-deposited alloy library. From bottom left to upper right, the FWHM decreases gradually. Comparing with the variation trend of the composition, it appears that the concentration of Fe and Cr play a minor role on the variation of FWHM, while the FWHM is positively related with the concentration of Mo. To validate these observations, the compositions of representative samples with varied FWHM (samples #58, #25, #45, #55, #9, and #39) were used to prepare rod samples for critical diameter analysis. Fig. 3d presents the XRD patterns of the six representative rods with different diameters, and the detailed data are shown in Table S5. Samples #58, #25, and #45, which exhibit larger FWHM values (0.457, 0.491, and 0.424), maintain amorphous structure with diameters equal or above 2 mm. Crystalline phases are detected for samples #55, #9, and #39 even with diameters of 1 mm or 1.5 mm, indicating a decline in the GFA of corresponding alloys. The critical diameter analyses confirm the validity of the relationship between GFA and FWHM. The result that GFA strongly correlates with the increasing Mo concentration is consistent with the literature that Mo plays a critical role in stabilizing the amorphous structure through significant atomic size mismatch effect [33].

To analyze the corrosion resistance of the 69 Fe-Cr-Mo-C-B alloys, the potentiodynamic polarization measurements were performed on each sample in 3.5 wt% NaCl solution at room temperature. Fig. 4a-c show the contour plots of the derived E_{corr}, i_{corr}, and passivation current density (i_{pass}) for the 69 alloys. As the contents of B and C have little variation across the material library, the compositions of Fe, Cr, and Mo were normalized accordingly, and the corresponding pseudo-ternary diagrams were also constructed, as presented in Fig. S5. The electrochemical properties exhibit obvious variations with the alloy composition. Generally, a smaller i_{corr} and i_{pass}, together with a higher E_{corr} indicate higher chemical stability of the materials and lower corrosion

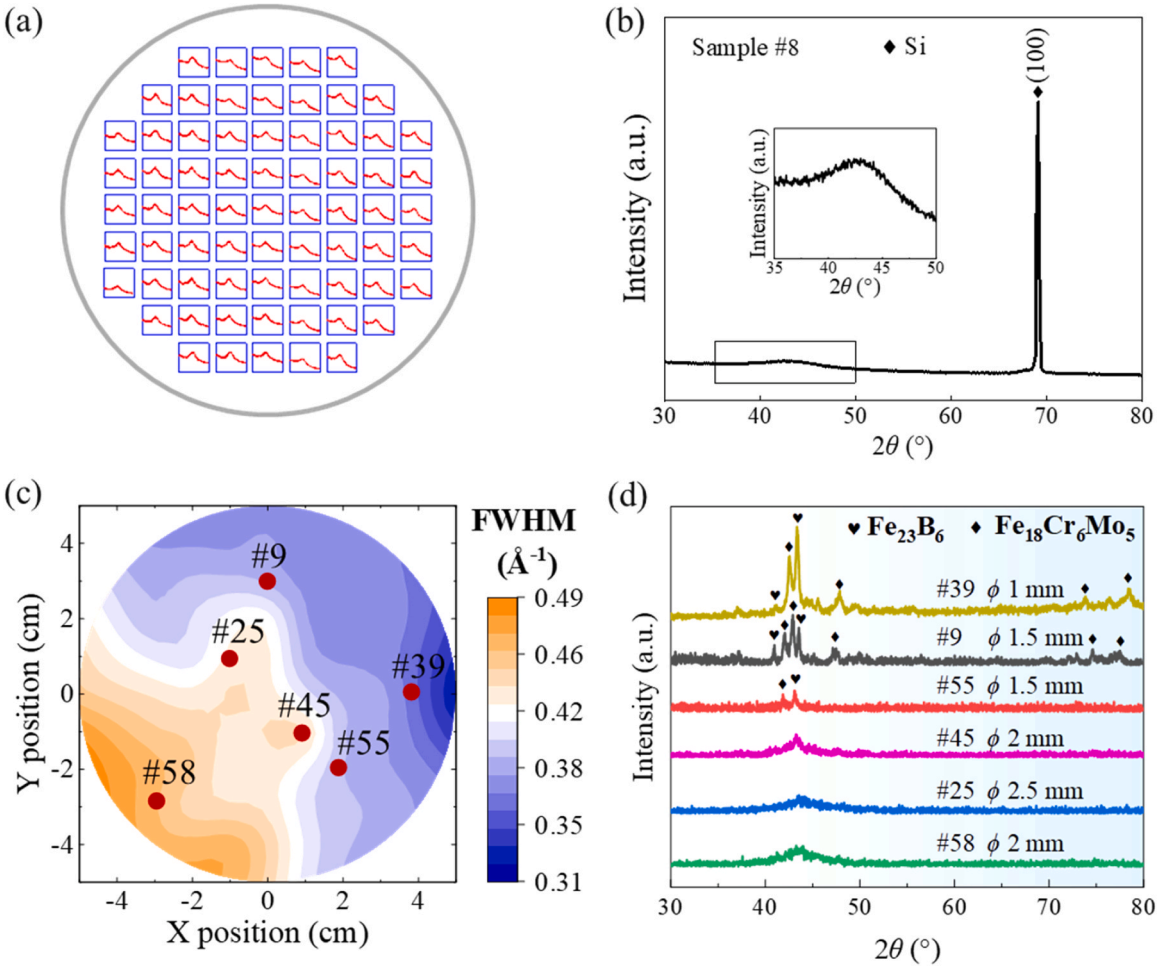

Fig. 3. (a) XRD patterns of the materials library. (b) XRD pattern of sample #8. (c) Contour plots for the FWHM of the materials library. (d) XRD patterns for 6 representative rod samples labeled in (c).

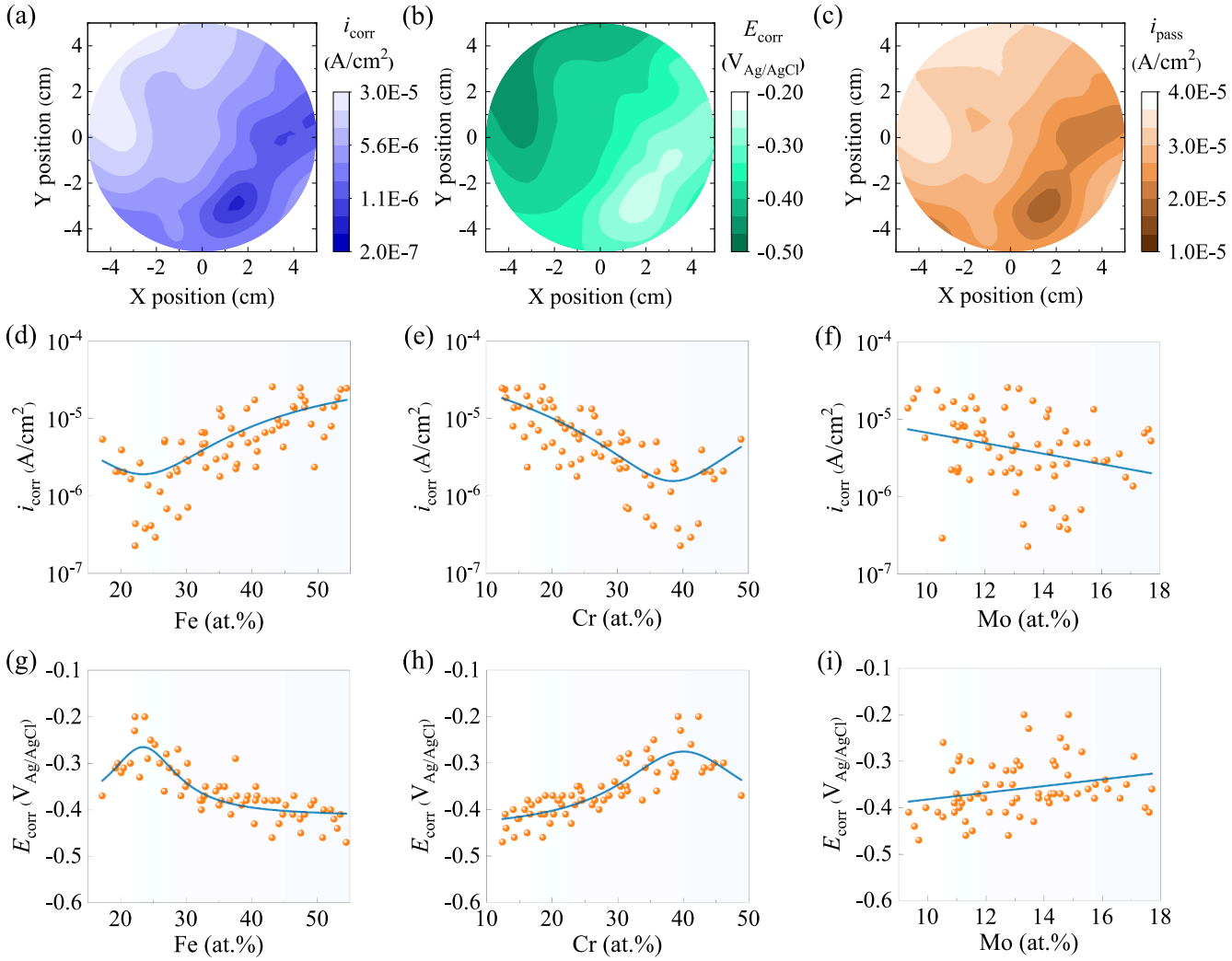

Fig. 4. Contour plots for the (a) corrosion current density, (b) corrosion potential and (c) passive current density. (d)-(f) The corrosion current density variation with the composition of Cr, Fe, and Mo, respectively. (g)-(i) The corrosion potential changes with Cr, Fe, and Mo, respectively.

rates [34]. As shown in Fig. 4b, the measured i_{corr} varies by two orders of magnitude across the 69 alloys, indicating their distinctly different corrosion behaviors. Within the combinatorial materials library, the alloys with higher Fe content and lower Cr content exhibit higher current density, suggesting that they are less resistant to corrosion in the 3.5 wt% NaCl solution. Similarly, the i_{pass} follows the same trend as the i_{corr} (Fig. 4c), further indicating the improved passivation behavior in Cr-rich alloys. The overall tendency of corrosion resistance revealed by E_{corr} is consistent with that by i_{corr} and i_{pass}. As shown in Fig. 4a, the measured corrosion potential is lower for the alloys with higher Fe content and lower Cr content. High corrosion potential appears in the Cr-rich region, suggesting their higher corrosion resistance. It is worth mentioning that the area with the highest Cr content is not the area with the best corrosion resistance.

To further investigate the influence of metallic elements on corrosion behavior of the Fe-Cr-Mo-C-B alloys, the variations of i_{corr} and E_{corr} with the content of each metallic element were derived from the contour plots. It can be seen that, the i_{corr} decreases from above $\sim 10^{-5}$ to below 10^{-7} A/cm^2 with the increase of Cr from 12 to 49 at% (Fig. 4e). Different from the trend observed in the variation of i_{corr}, the E_{corr} vs. Cr content indicates that higher Cr content can significantly increase E_{corr} with Cr content up to 39 at%, but decreases beyond this threshold (Fig. 4h). Among all samples, Cr39-film exhibits the highest corrosion potential and the lowest corrosion current density, indicating the best corrosion resistance. Fig. 4d and g display the i_{corr} and E_{corr} as a function of Fe content, which exhibit an antipodal tendency compared with Cr. And the highest chemical stability of the studied materials and lowest corrosion rates are reached at Fe content around 24 at%. Different from the trends observed in the variation of i_{corr} and E_{corr} with Cr and Fe, the values of i_{corr} and E_{corr} don't change much with Mo content (Fig. 4f and i). The above results indicate that the corrosion resistance of the alloys strongly relies on the concentration of Fe and Cr. In contrast, Mo plays a minor role in the variation of corrosion resistance.

3.2. Machine learning

The internal impact mechanism of the composition on the corrosion parameters (E_{corr}, i_{corr}) and GFA indicator (FWHM) is inherently complex and non-linear, as evidenced by the dataset obtained from high-throughput screening. To expand the materials library and improve prediction accuracy, a RFR model was implemented as it offers strong performance with small datasets and reduces overfitting risk through ensemble averaging. The specific workflow was illustrated in Fig. 5. Alloy properties are predicted using decision tree and random forest regression models. This approach enhances both the accuracy and robustness of the predictions. The 69 sets of data fitted in the model are shown in Fig. 6a, with the color of the balls representing the FHWM of the alloy, and their size corresponding to E_{corr} values. The predicted data

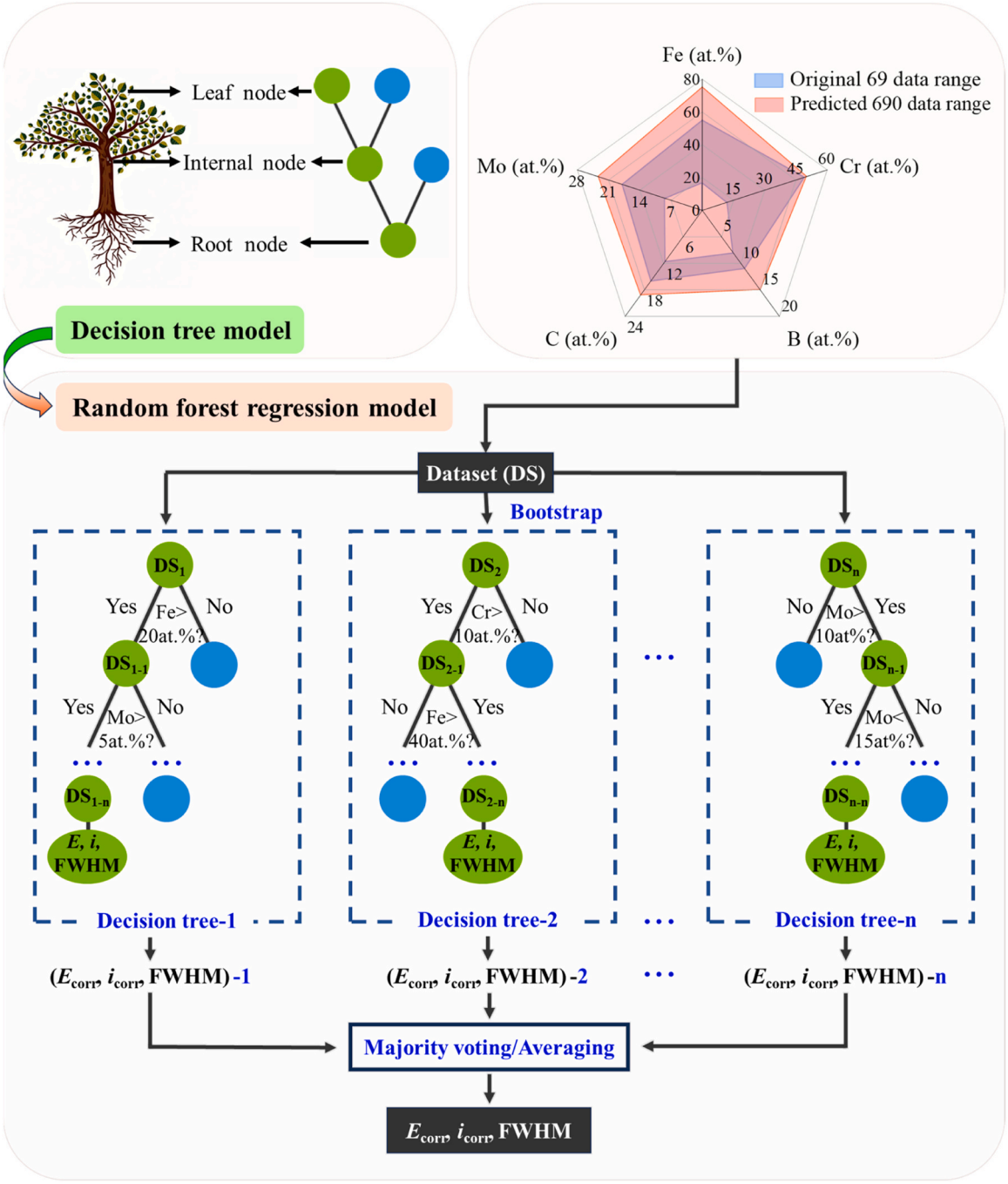

Fig. 5. Schematic of the machine learning-assisted design of Fe-Cr-Mo-C-B amorphous alloys. (a) Decision tree model. (b) Range of original data and predicted data, (c) Structure and working principle diagram of the random forest regression model.

obtained by RFR model are plotted in Fig. 6b. 690 set of data points were predicted. As the influence of Fe on FHWM is minor, and the impact of Fe on the E_{corr} is linear inversion with Cr, a 2D map was derived from the 3D map for a clearer illustration, as shown in Fig. 6c. The interspersed regions of the red and blue ovals in Fig. 6c identify alloy compositions exhibiting both elevated E_{corr} and increased FWHM, indicative of superior performance in terms of corrosion resistance and glass-forming ability. The modeling and prediction of i_{corr} are shown in Fig. S6, exhibiting similar results. The compositions of the 11 alloys within this region are listed in Table S6. Based on the predicted results, the metal element concentration gradients for alloys exhibiting excellent overall performance are as follows: the Cr concentration ranges from 28 to 35 at %, the Mo concentration ranges from 13 to 19 at%, and the Fe concentration ranges from 28 to 41 at%. These results suggest that the Fe content has a minimal impact on the overall performance of the alloy, while the concentrations of Cr and Mo play a significant role in determining the alloy's corrosion resistance and GFA. To further assess the reliability of the RFR model, we used it to predict the performance of the original 69 compositions. The predicted values showed good agreement with the experimental results. Fig. 6d-f present the prediction errors for E_{corr}, i_{corr}, and FWHM, respectively, demonstrating that the deviations between predicted and actual values are small, which further confirms the accuracy and robustness of the model. The MSE values of 0.00054, 0.00024, and 0.00052 were obtained from three independent prediction evaluations, demonstrating the model's robustness and the absence of overfitting. These results confirm the robustness and predictive accuracy

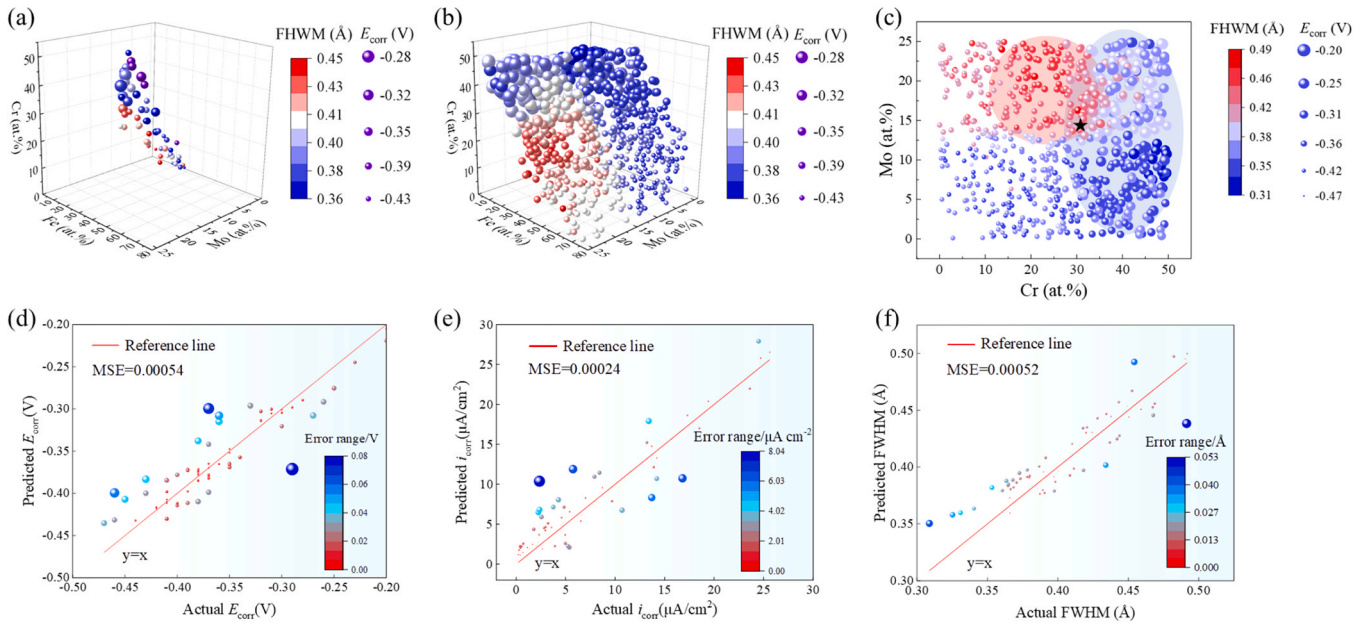

Fig. 6. (a) The raw data and (b, c) predicted data obtained by RFR model, the pentagram in (c) represents the composition for the coating preparation. The error map of RFR model for predicting the (d) E_{corr}, (e) i_{corr} and (f) FWHM.

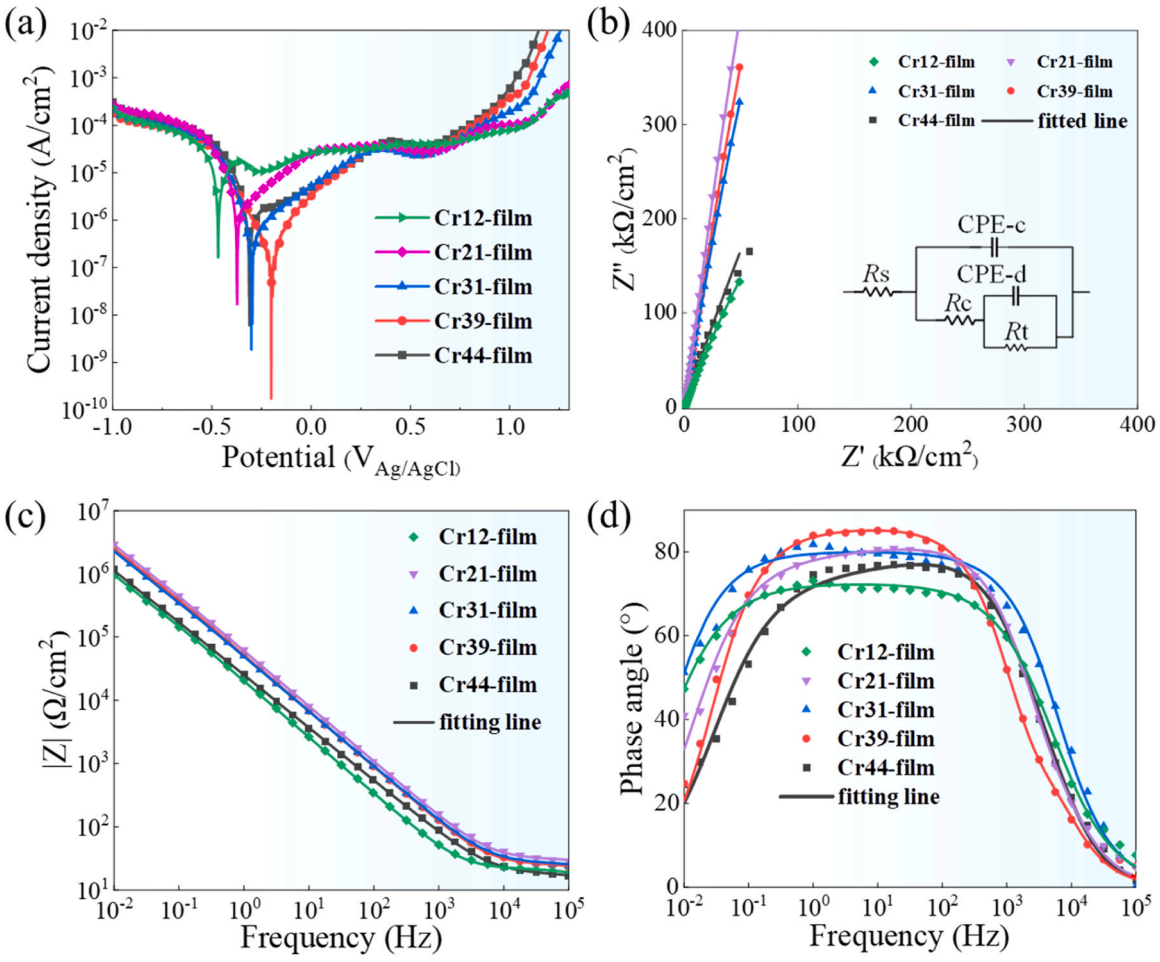

Fig. 7. (a) Potentiodynamic polarization plots, (b) Nyquist plots (the insets are equivalent circuit models), (c)Bode impedance, (d) Bode phase angle plots of the film samples in 3.5 wt% NaCl solution.

of the RFR approach for modeling the complex relationships among E_{corr}, i_{corr}, FWHM, and composition.

3.3. Structure and property of representative films with varied Cr concentration

To investigate the effect of the Fe/Cr ratio on corrosion behavior, five representative Fe-Cr-Mo-C-B amorphous alloys, which are located along the diagonal line between the FeCB and CrCB targets, were selected with systematically varied Cr contents: Cr12-film ($Fe_{55}Cr_{12}Mo_{10}C_{14}B_9$, #6), Cr21-film ($Fe_{41}Cr_{21}Mo_{14}C_{15}B_9$, #25), Cr31-film ($Fe_{31}Cr_{31}Mo_{14}C_{14}B_{10}$, #45), Cr39-film ($Fe_{24}Cr_{39}Mo_{15}C_{13}B_9$, #55), and Cr44-film ($Fe_{19}Cr_{44}Mo_{12}C_{15}B_{10}$, #64). As the Cr content increased, the Fe content was proportionally reduced, while the concentrations of Mo, C, and B were kept within a narrow range to maintain overall compositional balance. The potentiodynamic polarization curves, Nyquist plots, Bode impedance plots and Bode phase angle plots of the five samples are shown in Fig. 7, with the data values listed in Table S7 and S8. It can be seen that the Cr39-film exhibits superior corrosion performance, with the noblest E_{corr} of −0.21 $V_{Ag/AgCl}$, the lowest i_{corr} of 2.06×10^{-6} A/cm^2, and the lowest i_{pass} of 1.59×10^{-5} A/cm^2, respectively. The Nyquist plots in Fig. 7b show that the capacitive arc diameter of the Nyquist plots for Cr39-film is much larger than that of others, which indicates the superior corrosion resistance of the Cr39-film. Corrosion behavior of the films can also be uncovered from Bode plots as shown in Fig. 7c-d. The Bode impedance plots reveal that all the films demonstrate resistive behavior towards high frequencies, while displaying capacitive behavior within intermediate and low frequencies. The high-frequency capacitive loops arise due to passive film resistance on the film while low-frequency loops are attributed to charge transfer resistance during the electrochemical reaction process. Obviously, the maximal phase angle and the highest impedance value indicate the remarkable corrosion resistance of the Cr39-film alloy.

The stability of the passive films on Cr12-film, Cr21-film, Cr31-film, Cr39-film, and Cr44-film was analyzed under potentiostatic mode at 1 $V_{Ag/AgCl}$, with the potentiostatic polarization curves shown in Fig. S7a. In the initial stage of polarization, the current densities of all the films decline rapidly, and then gradually stabilize due to the formation of passive films [35–37]. Compared to Cr12-film and Cr44-film, the Cr21-film, Cr31-film and Cr39-film have lower current density, revealing their higher passive film stability, which is consistent with the potentiodynamic polarization results in Fig. 7a. With increasing test time, the current densities of Cr12-film and Cr44-film exhibit pronounced fluctuations in response to the alternating growth and

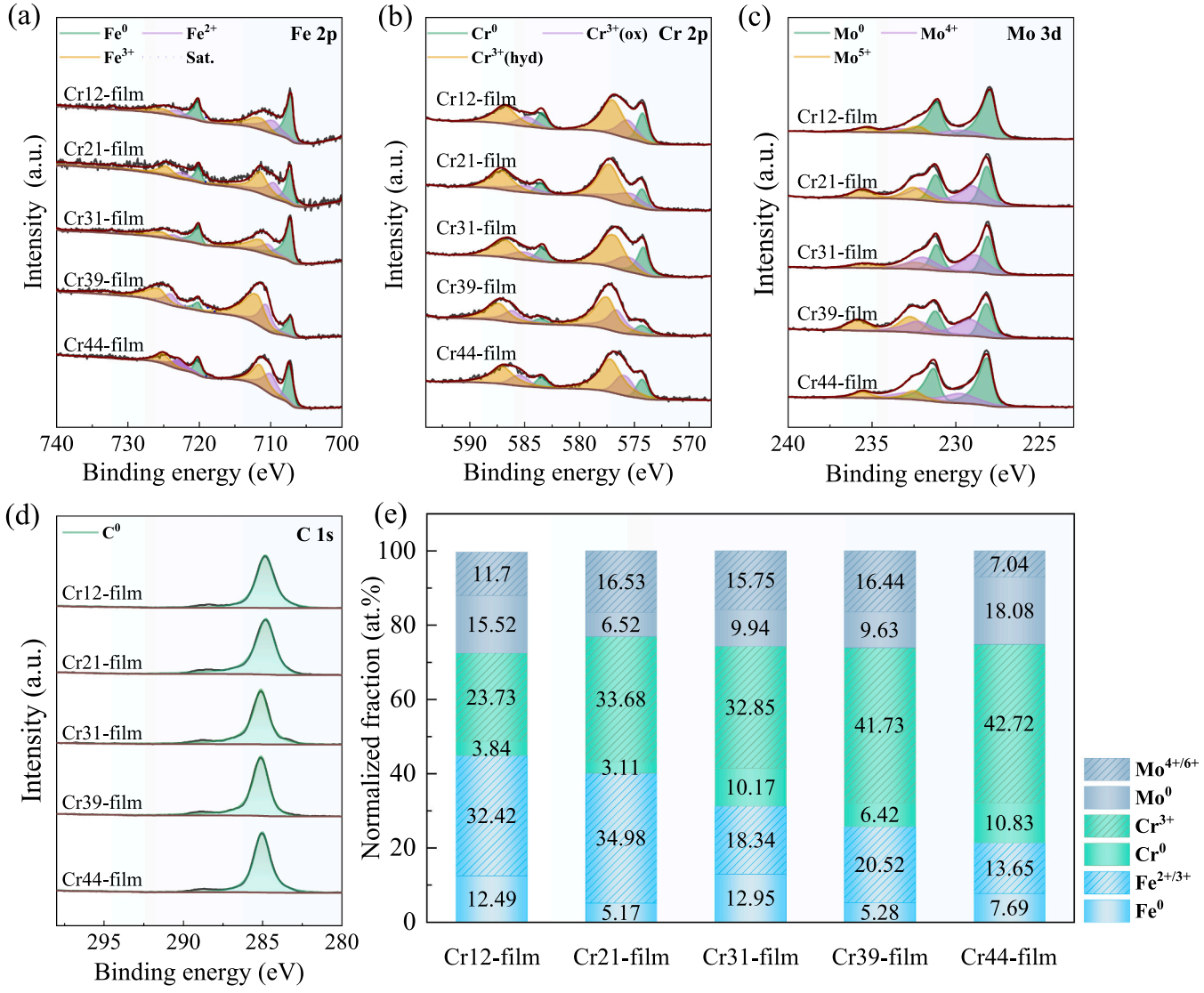

Fig. 8. XPS spectra of film samples after immersing in 3.5 wt% NaCl solution for 24 h. (a) Fe 2p, (b) Cr 2p, (c) Mo 3d and (d) C 1 s. (e) Fractions of cationic and metallic species in the passive films.

destruction of passive films, suggesting an inhomogeneous passive films growth. In contrast, the current densities of Cr21-film, Cr31-film, and Cr39-film remain nearly constant, indicating a balance between passive film growth and dissolution.

Furthermore, the surface morphologies of the Cr12-film, Cr21-film, Cr31-film, Cr39-film and Cr44-film after potentiostatic polarization at 1 $V_{Ag/AgCl}$ for 1 h were analyzed using SEM. As shown in Fig. S7b, the Cr12-film exhibits serious corrosion damage with the spalling of the passive film. For Cr21-film, the passive film looks almost intact, but dense corrosion products are observed on the surface (Fig. S7c). Different from the damaged passive films of Cr12-film and Cr21-film, no obvious defect can be observed on the surface of Cr31-film (Fig. S7d) or Cr39-film (Fig. S7e), indicating the passive films are dense and stable. However, as Cr content increases further, large cracks appear on the surface of Cr44-film (Fig. S7f), suggesting that the passive films are more easily destructed.

To understand the effects of alloy elements on passivity, XPS analysis was conducted on the surfaces of Cr12-film, Cr21-film, Cr31-film, Cr39-film, and Cr44-film. This analysis focuses on the metallic elements, as they play a critical role in the formation of oxide films. Fig. 8a-d present the Fe 2p, Cr 2p, Mo 3d, and C 1 s spectra for these alloys. For all five samples, the Fe 2p spectrum shows both metallic Fe (Fe^0) and oxidized Fe ($Fe_{(ox)}$). Additionally, the Fe 2p spectrum shows a Fe^{2+} satellite peak at 719.1 eV. The Cr 2p spectrum consists of three components: metallic Cr, Cr^{3+} (ox), and Cr^{3+} (hyd), as shown in Fig. 8b. Fig. 8c displays the Mo 3d spectra, which also split into three components: metallic Mo, Mo^{4+}, and Mo^{6+}. The relative amounts of Fe, Cr, and Mo in the surface oxide films were calculated based on peak areas and relative sensitivity factors, with the results summarized in Fig. 8e. It can be seen that with the increase of Cr content, the oxidation state of Cr also gradually increased, while the oxidation state of iron generally showed a downward trend. Based on the metal-oxygen bond strength and the metal-metal bond strength among metallic elements, it is much easier for Cr to get oxidized [38]. Besides, Cr is a key passivation element that contributes to the high corrosion resistance, while Mo stabilizes the passive films by preventing Cr dissolution during the passive process and enriching the passive films with Cr [38–40]. Therefore, the lowest content of Cr in the passive films for Cr12-film alloy is consistent with the worst corrosion resistance. However, the Cr44-film with dramatically reduced corrosion resistance exhibits the highest content of Cr. As shown in Fig. 8e, although the passive films of the Cr44-film have a higher content of Cr ions, the Mo ions display a drastic decline compared with the Cr39-film, and lower Mo content can lead to a decrease in the density of the passive films. The passive films of the Cr39-film, with higher Cr and Mo contents, are more stable and dense, effectively inhibiting further dissolution.

As tribological properties of alloys are closely related to hardness H, reduced modulus E_r, plasticity, and crack resistance [41–43], nanoindentation tests with partial unloading mode was carried out on the films to evaluate the H and E_r values, with the hardness-displacement curves shown in Fig. 9a. To avoid the influence of the substrate, the average hardness was calculated based on the values obtained at displacement between 70 and 120 nm, as highted by the yellow square in Fig. 9a. 6 nanoindentation tests were carried out of each film, with the hardness-displacement curves shown in Fig. S8. As shown in Fig. 9b, the hardness of the films, which are average values from the 6 tests, increases linearly with increasing Cr content. This can be attributed to the compositional effect, as Cr is harder than Fe. Furthermore, the E_r^2/H values, which has been demonstrated to be strongly related to both fracture toughness and wear resistance, were obtained from the nanoindentation tests [44]. The E_r^2/H values also increase with Cr content, indicating that the films with higher Cr content are more crack-resistant and may exhibit better wear resistance.

It is interesting to find a decline of the corrosion resistance from the Cr39-film to the Cr44-film. To uncover the underlying mechanism, the HADDF and EDS analyses were carried out on the cross-section of the Cr39-film and the Cr44-film. As shown in Fig. 10a, the HAADF image of the Cr39-film exhibits a completely uniform microstructure. The EDS mappings reveal that the Cr39-film displays homogeneous elemental distribution without any obvious segregation. Besides, the EDS line scanning along the yellow arrow in Fig. 10a further confirms the homogeneous elemental distribution of Cr, Fe, and Mo in the Cr39-film, as shown in Fig. 10b. The elements B and C are not shown due to the equipment's limitations in detecting these light elements. Different from the Cr39-film, the Cr44-film exhibits a distinct layered structure (Fig. 10c). As shown in Fig. 10d, the EDS line scanning along the yellow arrow in Fig. 10c reveals that the light and dark contrasts are due to Cr segregation. The segregation of Cr elements results in the formation of Cr-poor and Cr-rich regions, making the alloy more prone to corrosion.

The HRTEM images of the Cr39-film and Cr44-film samples are shown in Fig. 11, with SAED images shown in the inset. As no crystalline lattice is observed in the HRTEM images, and no sharp diffraction rings in the SAED patterns are observed, the amorphous features of the two samples can be confirmed. In order to statistically compare the structural disordering degree of the Cr39-film and Cr44-film, the areal fraction of the crystal-like order (CLO) regions was calculated by analyzing the 2D auto-correlation transformation of the divided cells (2 nm x 2 nm) for the two films, as shown in Fig. 11c-d. A cell is considered a CLO region if its auto-correlation pattern exhibits translational symmetry [45]. If the autocorrelation shows a maze-like pattern, the area is considered to be disordered. Red squares are used to highlight the areas of the CLO region, as shown in Fig. 11c and d. According to the statistics analysis, the areal fraction of CLO regions in the Cr39-film is about 12 %, and increases distinctly to 32 % in the Cr44-film. As the homogeneous

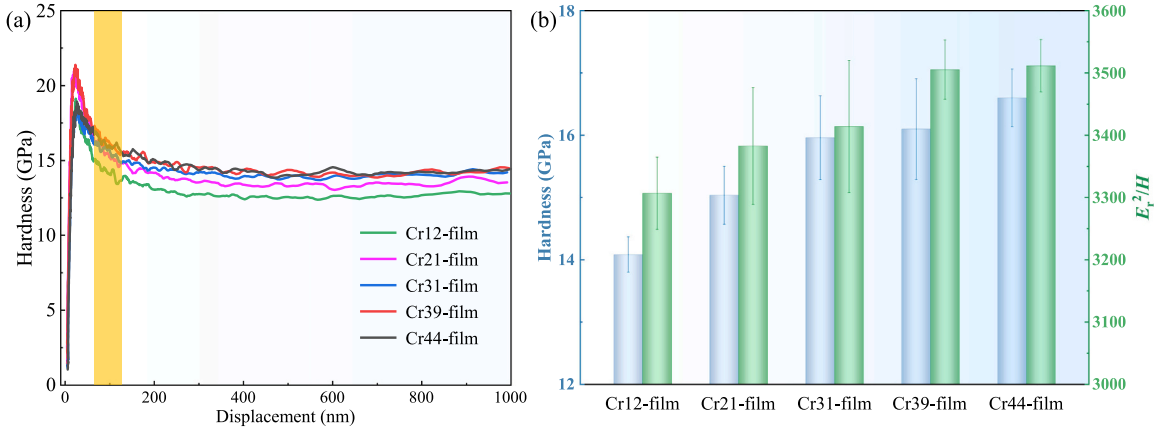

Fig. 9. Nanoindentation of film samples. (a) Hardness-displacement curves. (b) Hardness H and plasticity parameters E_r^2/H.

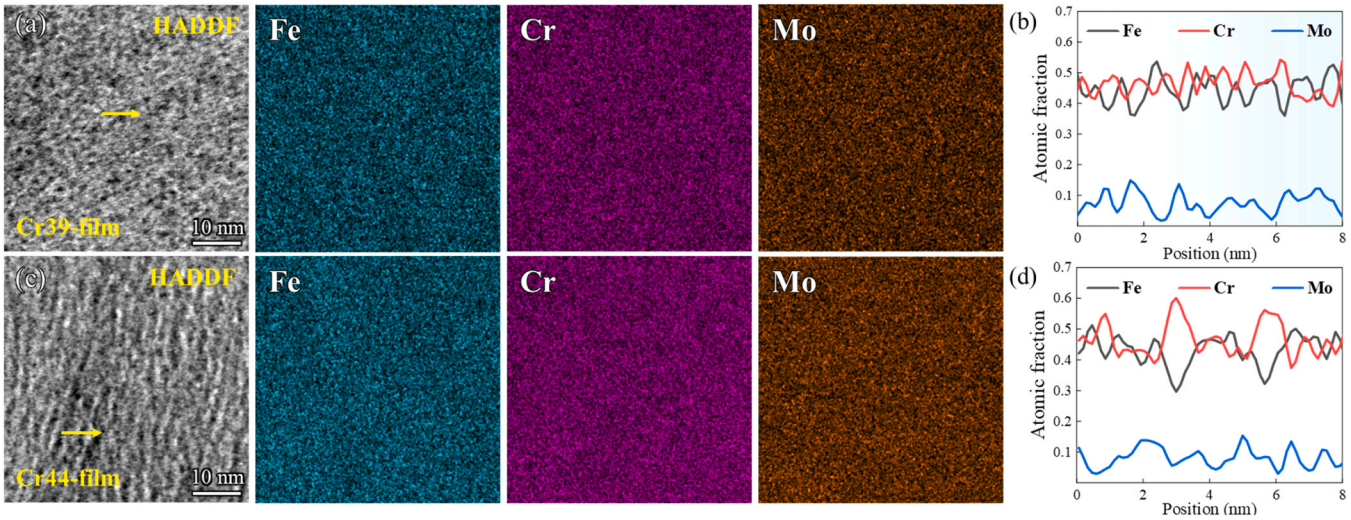

Fig. 10. (a) Dark-field (DF) TEM image of Cr39-film. (b) EDS line scan along the yellow arrow in (a). (c) Dark-field (DF) TEM image of Cr44-film. (d) EDS line scan along the yellow arrow in (c).

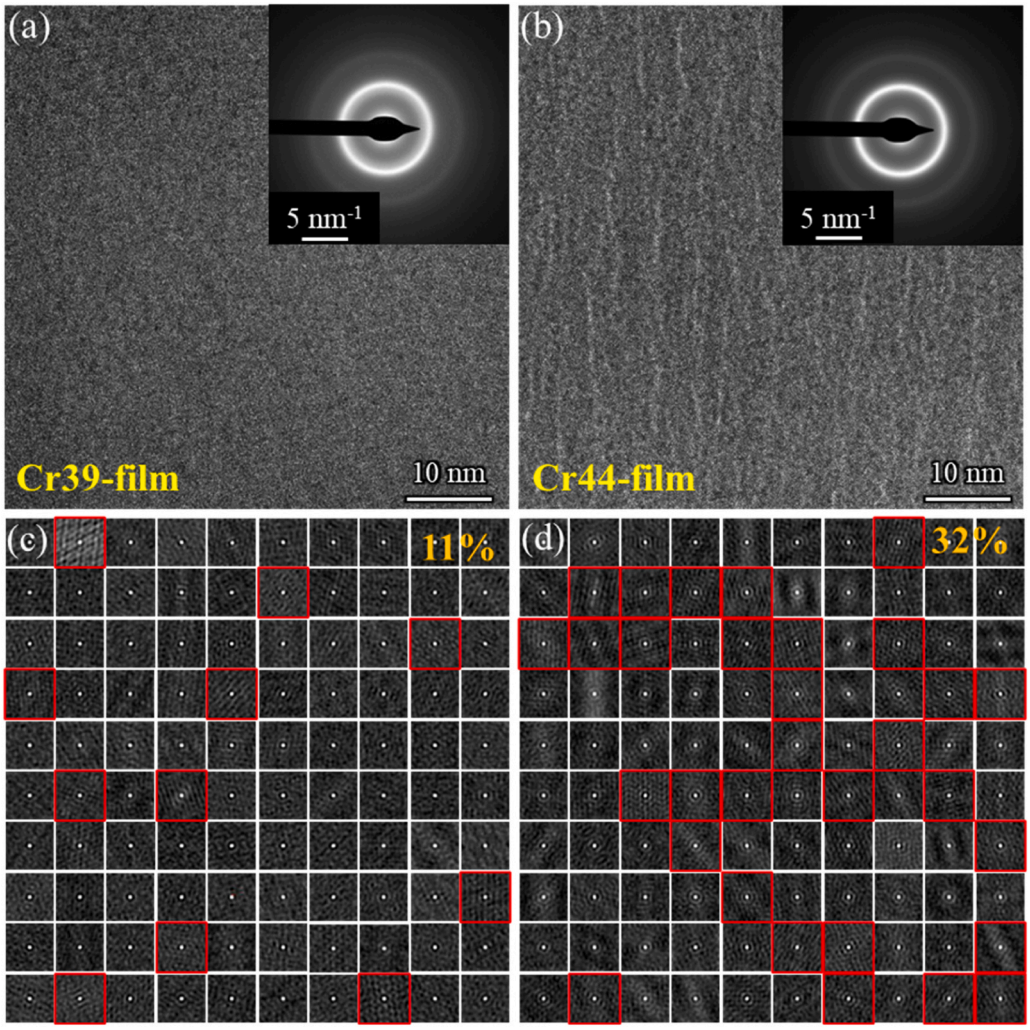

Fig. 11. HRTEM images and corresponding SAED patterns of (a) Cr39-film and (b) Cr44-film. 2D ACF analysis of (c) Cr39-film and (d) Cr44-film.

amorphous structure exhibits better corrosion resistance, the larger number of CLO regions in the Cr44-film is another reason for its declined corrosion performance.

The reduction of corrosion resistance in the Cr44-film with higher Cr content is consistent with that in stainless steels. For ferritic stainless steels, it's known that the Cr content is usually ranged from 11 to 30 at

%, and the excessive content of Cr in stainless steels will lead to the precipitation of Cr at grain boundary, which can seriously reduce corrosion resistance. The thin films deposited by magnetron sputtering at or near room temperature were reported to have extended solid solubilities as the arriving atoms do not have enough mobility to reach the correct positions [46–48]. Thus, the excellent corrosion resistance of Cr39-film with the Cr content as high as 39 at% results from the improved solid solubility. Although amorphous films do not exhibit grain boundary precipitation, excess Cr under sputtering conditions still induce nanoscale Cr-rich regions or short-range chemical ordering. These local fluctuations may influence the uniformity and protectiveness of the passive film. Therefore, the observed decrease in corrosion resistance in the Cr44-film is associated with local Cr enrichment exceeding the solubility limit.

3.4. structure and property of ribbons and coating

In order to verify the accuracy of the high-throughput screening and data-driven machine learning results, Cr12-ribbon, Cr21-ribbon, Cr31-ribbon, Cr39-ribbon and Cr44-ribbon samples were prepared via melt spinning, and their structure, thermal and corrosion behavior were analyzed. The ribbon of SAM1651 was also prepared for comparison. As shown in Fig. S9a, the XRD patterns of all the ribbons exhibit a wide hump without any sharp diffraction peaks, indicating that the ribbons are amorphous. Fig. S9b presents the DSC curves of the ribbons, and the thermal parameters were summarized in Table S9. It can be seen that the T_g increases from 810 to 955 K with the increasing of Cr content and the T_x increases gradually from 863 to 1005 K. While those values of SAM1651 are 841 K and 898 K. The higher T_g and T_x indicates the improvement of thermal stability. The wide supercooled liquid region (T_x-T_g) of the ribbons suggest that these alloys may have large GFA. For corrosion properties, a consistent trend can be observed in the ribbon samples as in the films in Fig. S10a, with the data values listed in Table S10 and S11. Cr39-ribbon alloy exhibits superior corrosion performance, with the maximal E_{corr} of 0.08 $V_{Ag/AgCl}$ and the lowest i_{corr} of 1.06×10^{-7} A/cm^2, respectively, while those values for SAM1651 are -0.27$V_{Ag/AgCl}$ and 2.05×10^{-7} A/cm^2. As shown in Fig. S10b, the capacitive arc diameter of Nyquist plots for all of the ribbons is larger than SAM1651, and Cr39-ribbon has the largest one. The analysis of Bode impedance plots (Fig. S10c) and Bode phase angle plots (Fig. S10d) also confirm that Cr39-ribbon has the best corrosion resistance. These results validate the reliability of the composition-corrosion relationship derived using the high-throughput method.

Furthermore, the $Fe_{31}Cr_{31}Mo_{14}C_{14}B_{10}$ composition (Sample #45, as shown in Table S3, corresponds to the composition represented by the pentagram in Fig. 6c), which exhibited superior comprehensive properties, including large GFA, good corrosion resistance, and high hardness, was selected for coating preparation using HVOF spraying. Fig. 12a shows the surface morphology of the gas atomized powders, which exhibit good sphericity. Fig. 12b presents the cross-sectional morphology of the Cr31-coating prepared by HVOF. It can be observed that the coating thickness exceeds 300 μm, exhibiting a dense structure with no large-sized pores (tens of microns), indicating a low porosity. Fig. 12c shows that crystalline phases are detected on the XRD patterns of both the powder and the coating, with the coating exhibiting a higher amorphous content due to the higher cooling rate during its preparation. As shown in Fig. 12d, the coating exhibits superior corrosion performance compared with 304 SS, with high E_{corr} of −0.34 $V_{Ag/AgCl}$ (equivalent to −0.1 V_{SCE}), low i_{corr} of 1.4×10^{-6} A/cm^2, and the i_{pass} of 4.51×10^{-6} A/cm^2, respectively. Besides, the wear performance of the coating is also analyzed and compared with the substrate materials. As shown in Fig. 12e and f, the wear rate of the coating is approximately 6×10^{-7} mm^{3}N^{-1}m^{-1}, comparable to the wear rate of diamond-like carbon materials [49]. The corrosion potential and wear rate of coating are compared with Fe-based amorphous coatings, Ni-based alloy coatings, Zr-based alloy coatings and high-entropy alloy coatings that have been reported, as shown in Fig. 13, and the specific details are presented in Table S12. The coating exhibits superior comprehensive performance, combining excellent corrosion resistance and exceptional wear resistance, outperforming most of the reported works, including SAM1651 and SAM2X5. Although the FeNiCrMoCBPNb HVAF coating exhibited a higher E_{corr} than our coating, its material cost is much

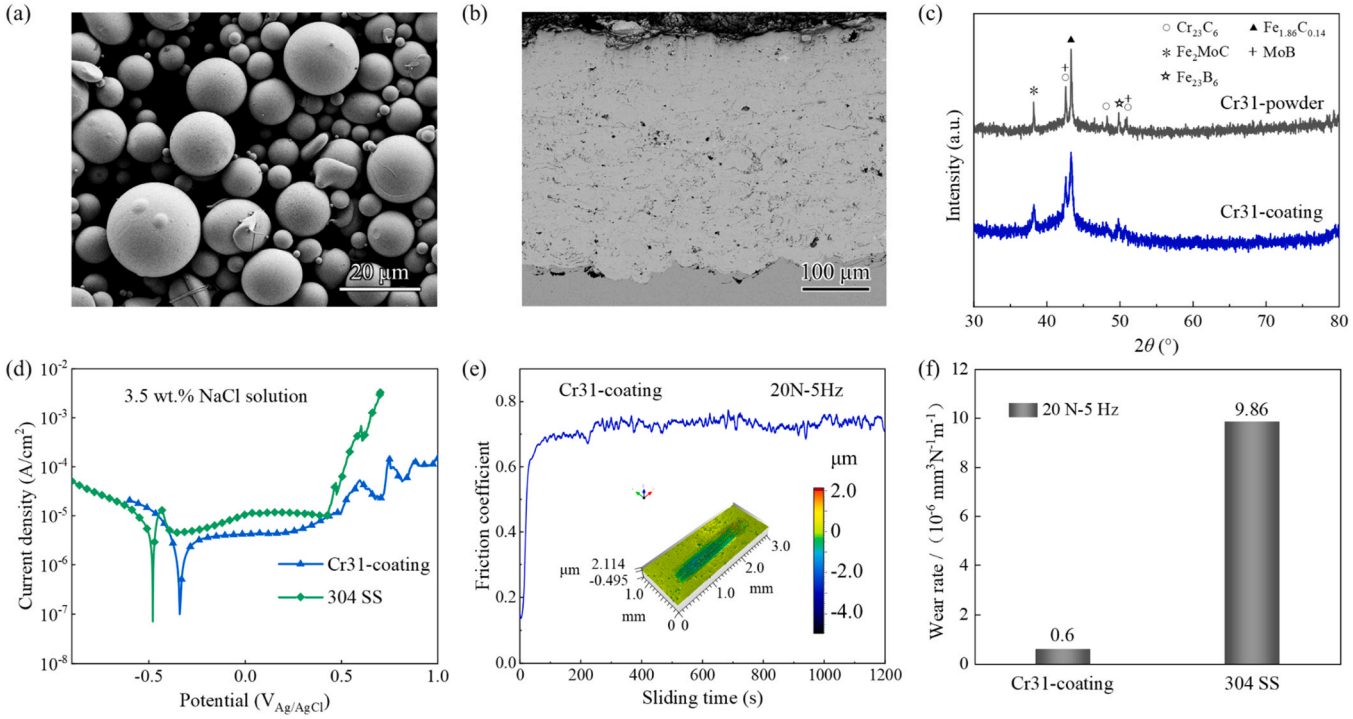

Fig. 12. SEM image of (a) Cr31-powder and (b) cross-section of Cr-31 coating. (c) XRD patterns of Cr31-powder and Cr31-coating. (d) Potentiodynamic polarization plots in 3.5 wt% NaCl solution. (e) Friction coefficient and 3D contour diagram. (f) Wear rate of Cr31-coating.

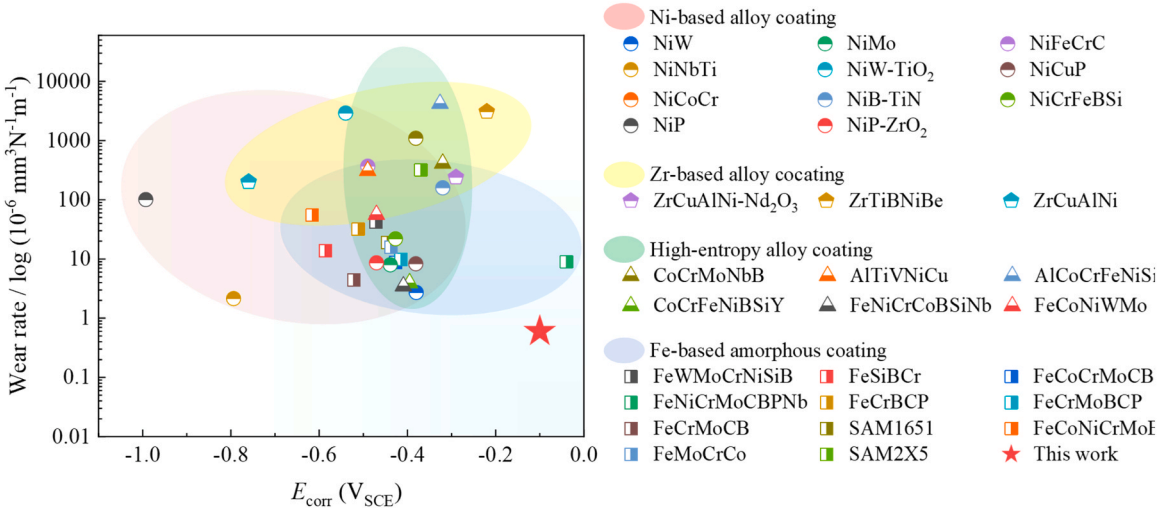

Fig. 13. Comparison of different material categories in terms of corrosion potential and wear resistance. Various markers and colors represent distinct material systems, including Fe-based amorphous coatings, Ni-based alloy coatings, Zr-based alloy coatings and high-entropy alloy coatings.

higher, and the content P may volatilize during spraying. This indicates that the high-throughput method developed in this study provides an effective approach for discovering high-performance alloys over a broad range of compositions, offering enhanced properties and a competitive edge.

4. Conclusions

In this work, the electrochemical corrosion behavior of Fe-Cr-Mo-C-B films in 3.5 wt% NaCl solution was systematically investigated using high-throughput methods combined with machine learning. The results indicated that the concentrations of Cr and Mo are the key factors influencing corrosion resistance and GFA, respectively. The good corrosion resistance of the alloy is attributed to the formation of a dense passivation layer, primarily contributed by the Cr content. However, excessive Cr content led to phase segregation, which reduced the corrosion resistance. The Cr31-coating exhibited remarkable overall performance, including E_{corr} of -0.34 $V_{Ag/AgCl}$, i_{corr} of 1.4×10^{-6}cm², and ultra-low wear rate of $6 \times 10^{-7}m^3N^{-1}m^{-1}$ outperforming most of the reported coatings. This work offers a powerful and efficient strategy for developing high-performance Fe-based amorphous coatings with enhanced corrosion and wear resistance, providing great potential for industrial applications.

CRediT authorship contribution statement

Fangkai Xiong: Methodology, Data curation, Writing – original draft, Investigation, Conceptualization. **Yuxi Qi:** Investigation. **Gaopeng Zou:** Conceptualization, Investigation. **Baosen Zhang:** Resources, Conceptualization. **Bo Sun:** Investigation, Conceptualization. **Tao Liang:** Conceptualization, Resources. **Shuaishuai Zhu:** Resources. **Xuhai Zhang:** Conceptualization, Resources. **Qiaoshi Zeng:** Conceptualization, Resources. **Baolong Shen:** Supervision, Funding acquisition, Project administration, Conceptualization. **Qianqian Wang:** Writing – original draft, Project administration, Conceptualization, Supervision, Funding acquisition.

Declaration of Competing Interest

The authors declare that they have no known competing financial interests or personal relationships that could have appeared to influence the work reported in this paper.

Acknowledgments

This work was supported by National Natural Science Foundation of China (52231005, 52571183), Jiangsu Provincial Key R&D Program (BE2021088), Open Research Fund of Jiangsu Key Laboratory for Advanced Metallic Materials (AMM2020A01, AMM2024A02, AMM2023B05), and Opening Project of Jiangsu Key Laboratory of Advanced Structural Materials and Application Technology (ASMA202302).

Appendix A. Supporting information

Supplementary data associated with this article can be found in the online version at doi:10.1016/j.corsci.2025.113450.

Data availability

Data will be made available on request.
Original data (Figshare)

References

[1] H. Li, Z. Lu, S. Wang, Y. Wu, Z. Lu, Fe-based bulk metallic glasses: glass formation, fabrication, properties and applications, Prog. Mater. Sci. 103 (2019) 235–318, https://doi.org/10.1016/j.pmatsci.2019.01.003.
[2] S.K. Nayak, A. Kumar, T. Laha, Fe-based metallic glass coatings by thermal spraying: a focused review on corrosion properties and related degradation mechanisms, Int. Mater. Rev. 68 (2023) 404–485, https://doi.org/10.1080/09506608.2022.2084670.
[3] D. Wang, S. Wang, J. Wang, Relationship between amorphous structure and corrosion behaviour in a Zr–Ni metallic glass, Corros. Sci. 59 (2012) 88–95, https://doi.org/10.1016/j.corsci.2012.02.017.
[4] Y.-C. Li, C. Zhang, W. Xing, S.-F. Guo, L. Liu, Design of Fe-based bulk metallic glasses with improved wear resistance, ACS Appl. Mater. Interfaces 10 (2018) 43144–43155, https://doi.org/10.1179/095066001225001067.
[5] F. Miao, Q. Wang, L.-C. Zhang, B. Shen, Magnetically separable Z-scheme FeSiB metallic glass/g-C3N4 heterojunction photocatalyst with high degradation efficiency at universal pH conditions, Appl. Surf. Sci. 540 (2021) 148401, https://doi.org/10.1016/j.apsusc.2020.148401.
[6] Z. Jia, Q. Wang, L. Sun, Q. Wang, L.C. Zhang, G. Wu, J.H. Luan, Z.B. Jiao, A. Wang, S.X. Liang, Attractive in situ self-reconstructed hierarchical gradient structure of metallic glass for high efficiency and remarkable stability in catalytic performance, Adv. Funct. Mater. 29 (2019) 1807857, https://doi.org/10.1002/adfm.201807857.
[7] S.X. Liang, Z. Jia, Y.J. Liu, W. Zhang, W. Wang, J. Lu, L.C. Zhang, Compelling rejuvenated catalytic performance in metallic glasses, Adv. Mater. 30 (2018) 1802764, https://doi.org/10.1002/adma.201802764.
[8] C. Suryanarayana, A. Inoue, Iron-based bulk metallic glasses, Int. Mater. Rev. 58 (2013) 131–166, https://doi.org/10.1179/1743280412Y.0000000007.

[9] M.-X. Li, S.-F. Zhao, Z. Lu, A. Hirata, P. Wen, H.-Y. Bai, M. Chen, J. Schroers, Y. Liu, W.-H. Wang, High-temperature bulk metallic glasses developed by combinatorial methods, Nature 569 (2019) 99–103, https://doi.org/10.1038/s41586-019-1145-z.

[10] S. Yoon, C. Lee, H. Choi, Evaluation of the effects of the crystallinity of kinetically sprayed Ni–Ti–Zr–Si–Sn bulk metallic glass on the scratch response, Mater. Sci. Eng. A 449 (2007) 285–289, https://doi.org/10.1016/j.msea.2006.02.434.

[11] J. Farmer, J.-S. Choi, C. Saw, J. Haslam, D. Day, P. Hailey, T. Lian, R. Rebak, J. Perepezko, J. Payer, Iron-based amorphous metals: high-performance corrosion-resistant material development, Metall. Mater. Trans. A 40 (2009) 1289–1305, https://doi.org/10.1007/s11661-008-9779-8.

[12] J.F. Löffler, Bulk metallic glasses, Intermetallics 11 (2003) 529–540, https://doi.org/10.1016/s0966-9795(03)00046-3.

[13] A. Inoue, Stabilization of metallic supercooled liquid and bulk amorphous alloys, Acta Mater. 48 (2000) 279–306, https://doi.org/10.1016/s1359-6454(99)00300-6.

[14] D.D. Xu, B.L. Zhou, Q.Q. Wang, J. Zhou, W.M. Yang, C.C. Yuan, L. Xue, X.D. Fan, L. Q. Ma, B.L. Shen, Effects of Cr addition on thermal stability, soft magnetic properties and corrosion resistance of FeSiB amorphous alloys, Corros. Sci. 138 (2018) 20–27, https://doi.org/10.1016/j.corsci.2018.04.006.

[15] D.R. Maddala, R.J. Hebert, Sliding wear behavior of Fe50−xCr15Mo14C15B6Erx (x=0, 1, 2at%) bulk metallic glass, Wear 294-295 (2012) 246–256, https://doi.org/10.1016/j.wear.2012.06.007.

[16] L. Yi-Cheng, Z. Cheng, X. Wei, G. Sheng-Feng, L. Lin, Design of Fe-Based Bulk Metallic Glasses with Improved Wear Resistance, ACS Appl. Mater. Interfaces 10 (2018) 43144–43155, https://doi.org/10.1179/095066001225001067.

[17] AlanSavan RidhaZerdoumi, E.BatsaTetteh MarshalAmalraj, O.A. Krysiak FlorianLourens, J.R.C. Junqueira, WolfgangSchuhmann AlfredLudwig, Combinatorial screening of electronic and geometric effects in compositionally complex solid solutions toward a rational design of electrocatalysts, Adv. Energy Mater. 14 (2023), https://doi.org/10.1002/aenm.202302177.

[18] H. Joress, B.L. DeCost, S. Sarker, T.M. Braun, S. Jilani, R. Smith, L. Ward, K.J. Laws, A. Mehta, J.R. Hattrick-Simpers, A high-throughput structural and electrochemical study of metallic glass formation in Ni–Ti–Al, ACS Comb. Sci. 22 (2020) 330–338, https://doi.org/10.5281/zenodo.3871786.

[19] D. Sur, H. Joress, J. Hattrick-Simpers, J.R. Scully, A high throughput aqueous passivation testing methodology for compositionally complex alloys using a scanning droplet cell, J. Electrochem. Soc. 170 (2023) 081507, https://doi.org/10.1149/1945-7111/aceeb8.

[20] A. Datye, S.A. Kube, D. Verma, J. Schroers, U.D. Schwarz, Accelerated discovery and mechanical property characterization of bioresorbable amorphous alloys in the Mg–Zn–Ca and the Fe–Mg–Zn systems using high-throughput methods, J. Mater. Chem. B. 7 (2019) 5392–5400, https://doi.org/10.1039/c9tb01302d.

[21] D. Sur, E.F. Holcombe, W.H. Blades, E.A. Anber, D.L. Foley, B.L. DeCost, J. Liu, J. Hattrick-Simpers, K. Sieradzki, H. Joress, An experimental high-throughput to high-fidelity study towards discovering al–cr containing corrosion-resistant compositionally complex alloys, High. Entropy Alloy. Mater. 1 (2023) 336–353, https://doi.org/10.1007/s44210-023-00020-0.

[22] M.-X. Li, Y.-T. Sun, C. Wang, L.-W. Hu, S. Sohn, J. Schroers, W.-H. Wang, Y.-H. Liu, Data-driven discovery of a universal indicator for metallic glass forming ability, Nat. Mater. 21 (2022) 165–172, https://doi.org/10.1038/s41563-021-01129-6.

[23] L. Hu, F. Li, W. Xie, C. Wang, M. Li, G. Wang, Y. Liu, Combinatorial investigation on corrosion resistance of Ir-Ni-Ta alloys, Corros. Sci. 234 (2024) 112153, https://doi.org/10.1016/j.corsci.2024.112153.

[24] Y. Shi, B. Yang, P.D. Rack, S. Guo, P.K. Liaw, Y. Zhao, High-throughput synthesis and corrosion behavior of sputter-deposited nanocrystalline Alx (CoCrFeNi) 100-x combinatorial high-entropy alloys, Mater. Des. 195 (2020) 109018, https://doi.org/10.1016/j.matdes.2020.109018.

[25] W. Guo, Y. Wu, L. Shi, J. Jia, R. Wang, H. Bu, Z. Zhu, Y. Shao, K. Yao, Integrating ultra-high saturation magnetization intensity and extreme-low coercivity in FeCoBSiCu alloy assisted by machine learning, -120643, Acta Mater. 285 (2025) 120643, https://doi.org/10.1016/j.actamat.2024.120643.

[26] S.Y. T, B.H. Y, L.M. Z, W.W. H, Machine learning approach for prediction and understanding of glass-forming ability, J. Phys. Chem. Lett. 8 (2017) 3434–3439, https://doi.org/10.1038/187869b0.

[27] W. Guo, Y. Wu, L. Shi, J. Jia, R. Wang, H. Bu, Z. Zhu, Y. Shao, K. Yao, Integrating ultra-high saturation magnetization intensity and extreme-low coercivity in FeCoBSiCu alloy assisted by machine learning, Acta Mater. 285 (2025) 120643, https://doi.org/10.1016/j.actamat.2024.120643.

[28] Y. Liu, Z. Wang, Y. Wang, Y. Li, F. Zhao, Z. Zhang, X. Liu, Data-driven composition design and property optimization of solid solution and precipitation simultaneously strengthened non-oriented silicon steel, Mater. Des. 242 (2024) 113011, https://doi.org/10.1016/j.matdes.2024.113011.

[29] D. You, H. Zhang, S. Ganorkar, T. Kim, J. Schroers, J.J. Vlassak, D. Lee, Electrical resistivity as a descriptor for classification of amorphous versus crystalline phases of alloys, Acta Mater. 231 (2022) 117861, https://doi.org/10.1016/j.actamat.2022.117861.

[30] S. Ding, Y. Liu, Y. Li, Z. Liu, S. Sohn, F.J. Walker, J. Schroers, Combinatorial development of bulk metallic glasses, Nat. Mater. 13 (2014) 494–500, https://doi.org/10.1038/nmat3939.

[31] Z. Li, C. Zhang, L. Liu, Wear behavior and corrosion properties of Fe-based thin film metallic glasses, J. Alloy. Compd. 650 (2015) 127–135, https://doi.org/10.1016/j.jallcom.2015.07.256.

[32] Y. Liu, T. Fujita, D. Aji, M. Matsuura, M. Chen, Structural origins of Johari-Goldstein relaxation in a metallic glass, Nat. Commun. 5 (2014) 3238, https://doi.org/10.1038/ncomms4238.

[33] W.H. Wang, Roles of minor additions in formation and properties of bulk metallic glasses, Prog. Mater. Sci. 52 (2007) 540–596, https://doi.org/10.1016/j.pmatsci.2006.07.003.

[34] L. Hu, X. Liu, C. Liang, S. Zhao, T. Chen, J. Li, G. Le, F. Qu, Y. Zhou, L. Qi, Microstructure evolution and corrosion mechanism of laser cladded Zr-Cu-Ni-Al in-situ metallic glass matrix composite coatings, Surf. Coat. Technol. 409 (2021) 126908, https://doi.org/10.1016/j.surfcoat.2021.126908.

[35] S.-j Pang, C.-h Shek, T. Zhang, K. Asami, A. Inoue, Corrosion behavior of glassy $Ni_{55}Co_5Nb_{20}Ti_{10}Zr_{10}$ alloy in 1 N HCl solution studied by potentiostatic polarization and XPS, Corros. Sci. 48 (2006) 625–633, https://doi.org/10.1016/j.corsci.2005.02.013.

[36] M. Lohrengel, Thin anodic oxide layers on aluminium and other valve metals: high field regime, Mater. Sci. Eng. R Rep. 11 (1993) 243–294, https://doi.org/10.1016/0927-796X(93)90005-N.

[37] J. Schultze, M. Lohrengel, D. Ross, Nucleation and growth of anodic oxide films, Electrochim. Acta 28 (1983) 973–984, https://doi.org/10.1016/0013-4686(83)85175-5.

[38] P. Marcus, On some fundamental factors in the effect of alloying elements on passivation of alloys, Corros. Sci. 36 (1994) 2155–2158, https://doi.org/10.1016/0010-938X(94)90013-2.

[39] X. Li, C.L. Qin, H. Kato, A. Makino, A. Inoue, Mo microalloying effect on the glass-forming ability, magnetic, mechanical and corrosion properties of $(Fe_{0.76}Si_{0.096}B_{0.084}P_{0.06})_{100-x}Mo_x$ bulk glassy alloys, J. Alloy. Compd. 509 (2011) 7688–7691, https://doi.org/10.1016/j.jallcom.2011.04.081.

[40] S. Pang, T. Zhang, K. Asami, A. Inoue, Formation of bulk glassy $Fe_{75-x-y}Cr_xMo_yC_{15}B_{10}$ alloys and their corrosion behavior, J. Mater. Res. 17 (2002) 701–704, https://doi.org/10.1557/JMR.2002.0100.

[41] J. Archard, Contact and rubbing of flat surfaces, J. Appl. Phys. 24 (1953) 981–988, https://doi.org/10.1063/1.1721448.

[42] E. Hornbogen, The role of fracture toughness in the wear of metals, Wear 33 (1975) 251–259, https://doi.org/10.1016/0043-1648(75)90280-X.

[43] D. Rigney, J. Hirth, Plastic deformation and sliding friction of metals, Wear 53 (1979) 345–370, https://doi.org/10.1016/0043-1648(79)90087-5.

[44] J. Lai, W. Hu, A. Datye, J. Liu, J. Schroers, U.D. Schwarz, J. Yu, Revealing the relationships between alloy structure, composition and plastic deformation in a ternary alloy system by a combinatorial approach, J. Mater. Sci. Technol. 84 (2021) 97–104, https://doi.org/10.1016/j.jmst.2020.12.038.

[45] Q. Wang, C. Liu, Y. Yang, J. Liu, Y. Dong, J. Lu, The atomic-scale mechanism for the enhanced glass-forming-ability of a Cu-Zr based bulk metallic glass with minor element additions, Sci. Rep. 4 (2014) 4648, https://doi.org/10.1038/srep04648.

[46] G. Meng, Y. Li, F. Wang, The corrosion behavior of Fe–10Cr nanocrystalline coating, Electrochim. Acta 51 (2006) 4277–4284, https://doi.org/10.1016/j.electacta.2005.12.015.

[47] D. McIntyre, J.E. Sundgren, J. Greene, Growth, structure, and physical properties of single-phase metastable fcc $Cu_{1-x}Cr_x$ solid solutions, J. Appl. Phys. 64 (1988) 3689–3696, https://doi.org/10.1063/1.341412.

[48] S. Shin, M. Ray, J. Rigsbee, J. Greene, Growth of metastable $Cu_{1-x}Cr_x$ solid solutions by ion mixing during bias-sputter deposition, Appl. Phys. Lett. 43 (1983) 249–251, https://doi.org/10.1063/1.94315.

[49] F. Li, M. Li, L. Hu, J. Cao, C. Wang, Y. Sun, W. Wang, Y. Liu, Achieving diamond-like wear in Ta-Rich metallic glasses, Adv. Sci. 10 (2023), https://doi.org/10.1002/advs.202301053.